On the Analysis of Thin-Walled Beams Based on Hamiltonian Formalism*

Shilei Han† and Olivier A. Bauchau‡
†University of Michigan-Shanghai Jiao Tong University Joint Institute
Shanghai, China
‡Department of Aerospace Engineering, University of Maryland
College Park, Maryland 20742

Abstract

In this paper, the Hamiltonian approach developed for beam with solid cross-section is generalized to deal with beams consisting of thin-walled panels. The governing equations of plates and cylindrical shells for the panels are cast into Hamiltonian canonical equations and closed-form central and extremity solutions are found. Typically, the end-effect zones for thin-walled beams are much larger than those for beams with solid cross-sections. Consequently, extremity solutions affect the solution significantly. Correct boundary conditions based on the weak form formulation are derived. Numerical examples are presented to demonstrate the capabilities of the analysis. Predictions are found to be in good agreement with those of plate and shell FEM analysis.

1 Introduction

Thin-walled beams may be represented as an assembly of flat strips, or cylindrical shells, or both. Typically three length scales are involved: the wall thickness, which is far smaller than a representative dimension of the cross-section, the representative dimension of the cross-section, which is far smaller than the beam's length, and the beam's length. Due to these geometric characteristics, the deformation of thin-walled beams under load differs from that observed for beams with solid cross-sections. Under torsional loading, thin-walled beams may exhibit significant warping. Furthermore, if the cross-section is restrained from warping, axial and shear stresses develop, a phenomenon known as *constrained* or *nonuniform torsion*.

Thin-walled beam theories reduce the analysis of two-dimensional structures to one-dimensional problems that are far simpler to solve. Although more sophisticated formulations, such as those based on two-dimensional plate or shell finite element or finite strip methods, are able to capture the in-plane and out-of-plane warping behavior of thin-walled beams to the desired level of accuracy, the associated computational burden is often too heavy. Moreover, two-dimensional approaches do not provide an intuitive interpretation of the observed phenomena. The main goal of thin-walled beam theories is to approximate the assembly of two-dimensional plate and shell structures with one-dimensional models, while retaining an accurate representation of the local stress and strain fields over the contour of the cross-section.

Classical thin-walled beam theories have been proposed by Vlasov [1] and Benscopter [2, 3, 4] for isotropic thin-walled beams with open and closed cross-sections, respectively, based on kinematic

* *Computers & Structures*, **170**(1): pp 37-48, July 2016.

assumptions. In many applications, thin-walled beams are, in fact, complex built-up structures with layers of anisotropic material stacked through the thickness of the walls. This new type of structural component prompted the development of new thin-walled beam theories [5, 6, 7]. With the goal of capturing the intricate stress field that develops under load, further refinements then followed by introducing more cross-section warping modes [8]. Although these approaches lead to higher accuracy, the number of unknowns increases considerably; furthermore, the identification of the dominant modes is often arduous.

Efficient thin-walled beam models can be obtained more rigorously from two-dimensional plate and shell equations through dimensional reduction techniques that split the original problem into a one-dimensional analysis over the beam's span and a one-dimensional cross-sectional analysis along the section's contour. These approaches can handle thin-walled beams made of anisotropic composite materials without increasing the total number of unknowns.

Asymptotic and multiscale analysis methods have been the tools of choice for dimensional reduction. Berdichevsky [9] proposed the Variational Asymptotic Method (VAM), in which asymptotic analysis is applied to the energy functional. Classical and Reissner thin-walled composite beam models based on VAM were developed by Hodges *et al.* [10, 11].

It is not necessary to use asymptotic methods to tackle thin-walled beam problems. Beam equations can be obtained directly through a separation of variables approach over the span-wise and along the section's contour directions. An approach of this type is the Generalized Beam Theory (GBT) proposed by Schardt [12] and further developed by numerous authors [13, 14, 15, 16, 17, 18], among others. The formulations based on GBT provide a general procedure to determine the section's deformation modes. Projection of the governing equations onto these deformation modes leads to a unified and efficient one-dimensional beam formulation. This approach has been extended to buckling analysis (second-order GBT) and post-buckling analysis (third-order GBT).

A fundamental challenge in dimensional reduction of beam problems is to identify the algebraic structure of the cross-section's deformation modes and the characteristics of the corresponding solutions. Giavotto *et al.* [19] identified two types of solutions for beam problems: the central solutions, which are the solutions of Saint-Venant's problem, and the extremity solutions, which decay exponentially away from the beam's ends.

Mielke [20, 21] found that the solutions of Saint-Venant's problem correspond to the center manifold of the system, which is spanned by the twelve generalized eigenvectors associated with four distinct Jordan chains. Of these twelve generalized eigenvectors, six correspond to the beam's rigid-body modes while the others six are the fundamental deformation modes of the beam: extension, torsion, and bending and shearing in two directions.

Zhong [22] developed novel analytical techniques based on the Hamiltonian formalism. A Hamiltonian operator characterizes the stiffness of the structure and its null and purely imaginary eigenvalues give rise to the solution of Saint-Venant's problem. The eigenvalues presenting a non-vanishing real part give rise to decaying solutions. As previously stated by Mielke, Zhong also identified the Jordan chains associated with the eigenvalues of the Hamiltonian operator with a vanishing real part.

Bauchau and Han [23] developed a three-dimensional beam theory based on the Hamiltonian formalism. The approach proceeds through a set of structure-preserving transformations using symplectic matrices and decomposes the solution into its central and extremity components. The same authors further generalized the approach to initially curved beams undergoing large motion but small strains [24], and helicoidal beams subjected to distributed loads [25]. For beams with solid cross-sections, the non-vanishing eigenvalues are associated with very small end effect zones near the beam's ends [25].

In this paper, the Hamiltonian formalism is extended to thin-walled beam problems. Governing equations of plates and shells for the panels are cast into Hamiltonian canonical equations and closed-form central and extremity solutions are found based on a procedure similar to that used for

beams with solid-section. Typically, the end-effect zones for thin-walled beams are much larger than those for beams with solid cross-sections. Consequently, the extremity solutions should be taken into account because they alter the solution over the entire span of the beam. The other factor that makes extremity solutions important is the boundary condition. When subjected to twisting or shearing, thin-walled beams warp significantly. Far away from the end conditions, this warping if free to develop, but it is not consistent with built-in boundary conditions, a phenomenon known as "constrained warping effects." Saint-Venant's solution, which consists of the central solutions only, cannot predict constrained warping effects. Extremity solutions must be considered to satisfy the boundary constraints. In this paper, the boundary conditions are enforced in a weak sense, leading to a set of over-determined equations. Accurate predictions are obtained by combining central and extremity solutions, the latter are excited by the boundary conditions.

The following assumptions are made: *(1)* the straight thin-walled beam is an assembly of plates, or cylindrical shells, or both; *(2)* cross-sections of arbitrary geometry and material properties (heterogeneous and anisotropic) are considered, but remain uniform along the span; *(3)* strains and warping displacements remain small. Due to these assumptions, the governing equations of the problem can be cast into a homogenous Hamiltonian system with constant coefficients.

The paper is organized as follows: the kinematics of the problem and the governing equations of thin-walled beam problems are presented in sections 2 and 3, respectively. The algebraic structure of the solutions is the focus of section 4. The appropriate boundary conditions are derived in section 5 and numerical examples are presented in the last section.

2 Kinematics of the problem

Figure 1 depicts a straight thin-walled beam consisting of an assembly of plates and cylindrical shells, each of which is referred to as a panel. The beam's sectional contour, Γ, is the intersection of the cross-sectional plane with the panels' mid-planes. Let curve $\Gamma^{(i)}$ denoted the contour of the i^{th} panel. The straight reference line of the beam is denoted $\mathcal{C}$. Consider an arbitrary point $\mathbf{B}$, located at the intersection of the sectional plane with the reference line. Denote $\underline{r}_B$ the position vector of point $\mathbf{B}$ with respect to the origin of the inertial frame, $\mathcal{F} = [\mathbf{O}, \mathcal{I} = (\bar{\imath}_1, \bar{\imath}_2, \bar{\imath}_3)]$, and α_1 the arc-length coordinate along $\mathcal{C}$. The unit tangent vector to curve $\mathcal{C}$ is $\bar{b}_1 = \partial \underline{r}_B / \partial \alpha_1$. Because the plane of the cross-section is perpendicular to unit vector $\bar{b}_1$, a frame $\mathcal{F}_B = \left[\mathbf{B}, \mathcal{B}^* = (\bar{b}_1, \bar{b}_2, \bar{b}_3)\right]$ can be introduced which defines the position and orientation of the cross-section in the reference configuration, as illustrated in fig. 1. Basis $\mathcal{B}^*$ is referred to as sectional basis. In the sequel, notation $(\cdot)^*$ indicates tensor components resolved in the sectional basis $\mathcal{B}^*$.

2.1 Strain components

Consider an arbitrary material point of the beam, $\mathbf{P}$, located on contour $\Gamma^{(i)}$. Let $\underline{q}$ denote the relative position of point $\mathbf{P}$ with respect to point $\mathbf{B}$ and $\alpha_2^{(i)}$ the curvilinear coordinate measuring the arc length along curve $\Gamma^{(i)}$. A local basis, $\mathcal{B}^+ = (\bar{b}_1, \bar{t}^{(i)}, \bar{n}^{(i)})$, is introduced, where $\bar{t}^{(i)}$ and $\bar{n}^{(i)}$ are the unit tangent and normal vectors to $\Gamma^{(i)}$, respectively, as shown in fig. 1, *i.e.*, $\bar{t}^{(i)} = \partial \underline{q} / \partial \alpha_2^{(i)}$ and $\bar{n}^{(i)} = \bar{b}_1 \times \bar{t}^{(i)} = \tilde{b}_1 \bar{t}^{(i)}$, where notation $\tilde{(\cdot)}$ indicates the skew symmetric matrix constructed from the components of vector $(\cdot)$. Let ρ denote the radius of curvature of curve $\Gamma^{(i)}$, *i.e.*, $\rho = \bar{n}^{(i)T} \bar{t}^{(i)}_{,2}$. In the sequel, notation $(\cdot)^+$ indicates tensor components resolved in the local basis $\mathcal{B}^+$.

The infinitesimal displacement of a point of curve $\Gamma^{(i)}$ is denoted $\underline{u}^+ = \{u_1^+, u_2^+, u_3^+\}^T$ and the infinitesimal rotation of local basis $\mathcal{B}^+$ is $\underline{\theta}^+ = \{-\theta_2^+, \theta_1^+, \theta_3^+\}^T$. To be consistent with conventional plate and shell notations, rotations about axis $\bar{b}_1$ and $\bar{t}$ are denoted as $-\theta_2^+$ and θ_1^+, respectively. In linear shell theory, rotation about normal vector $\bar{n}$ is immaterial and is only active at the junctions

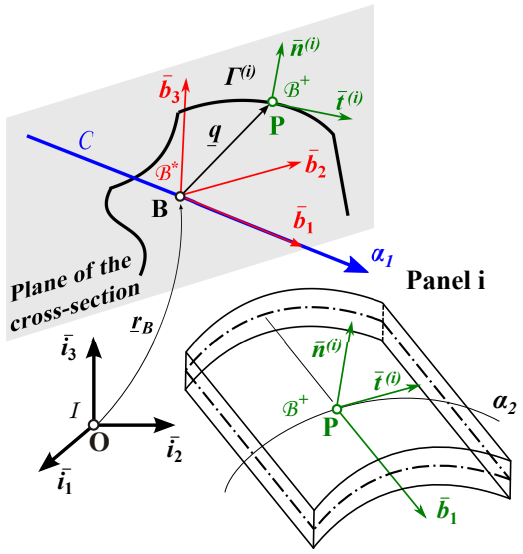

Figure 1: Configuration of a beam with thin-walled section.

between two or more panels, as discussed in section 3.2. The displacement and rotation fields are combined as $\underline{\mathfrak{u}}^{+T} = \{\underline{u}^{+T}, \underline{\theta}^{+T}\}$. The cylindrical panel's sectional strain components [26] are then $\underline{\mathfrak{e}}^{+} = \{u^{+}_{1,1},\, u^{+}_{2,2} + u^{+}_{3}/\rho,\, u^{+}_{1,2} + u^{+}_{2,1},\, u^{+}_{3,1} + \theta^{+}_{1},\, u^{+}_{3,2} + \theta^{+}_{2},\, \theta^{+}_{1,1},\, \theta^{+}_{2,2},\, \theta^{+}_{2,1} + \theta^{+}_{1,2}\}^{T}$, where notations $(\cdot)_{,1}$ and $(\cdot)_{,2}$ indicate partial derivatives with respect to span-wise variable α_1 and curvilinear coordinate $\alpha_2^{(i)}$, respectively. It can be expressed in a compact manner as

$$\underline{\mathfrak{e}}^{+} = \underline{\underline{A}}_1 \underline{\mathfrak{u}}^{+}_{,1} + \underline{\underline{A}}_2 \underline{\mathfrak{u}}^{+}_{,2} + \underline{\underline{B}}\, \underline{\mathfrak{u}}^{+}, \tag{1}$$

where matrices $\underline{\underline{A}}_1$, $\underline{\underline{A}}_2$, and $\underline{\underline{B}}$, all three of size 8×6, are defined in A.

2.2 Semi-discretization of the displacement and rotation field

The following semi-discretization of the displacement field of the i^{th} panel is performed

$$\underline{\mathfrak{u}}^{(i)+}(\alpha_1, \alpha_2^{(i)}) = \underline{\underline{N}}(\alpha_2^{(i)})\, \hat{\underline{\mathfrak{u}}}^{(i)}(\alpha_1), \tag{2}$$

where matrix $\underline{\underline{N}}(\alpha_2^{(i)})$ stores the one-dimensional shape functions used in the discretization and array $\hat{\underline{\mathfrak{u}}}^{(i)}(\alpha_1)$ stores the nodal values of the displacement and rotation fields. Notation $\hat{(\cdot)}$ indicates nodal quantities of the discretized variables. Let $\ell^{(i)}$ be the number of nodes of the i^{th} panel; hence, nodal array $\hat{\underline{\mathfrak{u}}}^{(i)}$ is of size $n^{(i)} = 6\ell^{(i)}$. Because the nodal rotation component θ_3^{+} is immaterial, the number of degrees of freedom at each node is $5n$.

Note that discretization (2) differs from those used in standard finite element procedures. In typical finite element discretization, the strip would be treated as a two-dimensional body and discretization (2) would be written as $\underline{\mathfrak{u}}^{(i)+}(\alpha_1, \alpha_2^{(i)}) = \underline{\underline{N}}(\alpha_1, \alpha_2^{(i)})\hat{\underline{\mathfrak{u}}}^{(i)}$, where matrix $\underline{\underline{N}}(\alpha_1, \alpha_2^{(i)})$ stores two-dimensional shape functions and $\hat{\underline{\mathfrak{u}}}^{(i)}$ the nodal values. In this case, the mesh would extend over the beam's cross-section and along its span. Array $\hat{\underline{\mathfrak{u}}}^{(i)}$ would store the nodal displacement at all nodes over the cross-section and along the beam's span, defining a full discretization of the structure.

Introducing this discretization into eq. (1) yields the components of the strain components as

$$\underline{\mathfrak{e}}^{+} = \underline{\underline{A}}_1 \underline{\underline{N}}\, \hat{\underline{\mathfrak{u}}}^{(i)\prime} + \underline{\underline{G}}\, \underline{\underline{N}}\, \hat{\underline{\mathfrak{u}}}^{(i)}, \tag{3}$$

where $\underline{\underline{G}} = \underline{\underline{A}}_2 \partial/\partial\alpha_2^{(i)} + \underline{\underline{B}}$. Because the displacement field has been discretized over the beam cross-section, only the derivative with respect to axial variable α_1 remains and for simplicity, it is denoted $(\cdot)'$.

3 Governing equations

The beam's governing equations will be derived based on the Hamiltonian formalism. The strain energy density of the system is derived in section 3.1, the assembly of panel's stiffnesses are considered in section 3.2, and at last, Hamilton's canonical equations are obtained.

3.1 Strain energy

The strain energy density per unit span of the beam for the i^{th} panel is

$$L^{(i)} = \frac{1}{2}\int_{\Gamma_i} \underline{\boldsymbol{\varepsilon}}^{+T}\underline{\mathfrak{f}}^{+}\ \mathrm{d}\alpha_2^{(i)} = \frac{1}{2}\int_{\Gamma_i} \underline{\boldsymbol{\varepsilon}}^{+T}\underline{\underline{\mathcal{D}}}^{(i)+}\underline{\boldsymbol{\varepsilon}}^{+}\ \mathrm{d}\alpha_2^{(i)}, \tag{4}$$

where array $\underline{\mathfrak{f}}^{+}$ stores the panel's stress resultants and matrix $\underline{\underline{\mathcal{D}}}^{(i)+}$ stores the components of its sectional stiffness matrix resolved the material basis. The cross-sectional distribution of materials is arbitrary but remains uniform along the beam's span. Introducing the discretized components of strain tensor given by eq. (3), the strain energy density becomes

$$L^{(i)} = \frac{1}{2}\left[\hat{\underline{\mathbf{u}}}^{(i)\prime T}\left(\underline{\underline{M}}^{(i)}\hat{\underline{\mathbf{u}}}^{(i)\prime} + \underline{\underline{C}}^{(i)T}\hat{\underline{\mathbf{u}}}^{(i)}\right) + \hat{\underline{\mathbf{u}}}^{(i)T}\left(\underline{\underline{C}}^{(i)}\hat{\underline{\mathbf{u}}}^{(i)\prime} + \underline{\underline{E}}^{(i)}\hat{\underline{\mathbf{u}}}^{(i)}\right)\right]. \tag{5}$$

Matrices $\underline{\underline{M}}^{(i)}$, $\underline{\underline{C}}^{(i)}$, and $\underline{\underline{E}}^{(i)}$, each of size $n^{(i)} \times n^{(i)}$, are

$$\underline{\underline{M}}^{(i)} = \int_{\Gamma^{(i)}} (\underline{\underline{A}}_1\ \underline{\underline{N}})^T\underline{\underline{\mathcal{D}}}^{(i)+}(\underline{\underline{A}}_1\ \underline{\underline{N}})\mathrm{d}\alpha_2^{(i)}, \tag{6a}$$

$$\underline{\underline{C}}^{(i)} = \int_{\Gamma^{(i)}} (\underline{\underline{A}}_1\ \underline{\underline{N}})^T\underline{\underline{\mathcal{D}}}^{(i)+}(\underline{\underline{G}}\ \underline{\underline{N}})\ \mathrm{d}\alpha_2^{(i)}, \tag{6b}$$

$$\underline{\underline{E}}^{(i)} = \int_{\Gamma^{(i)}} (\underline{\underline{G}}\ \underline{\underline{N}})^T\underline{\underline{\mathcal{D}}}^{(i)+}(\underline{\underline{G}}\ \underline{\underline{N}})\ \mathrm{d}\alpha_2^{(i)}. \tag{6c}$$

Given the distribution of material stiffness properties, these matrices can be evaluated by integration over curve $\Gamma^{(i)}$. Based the assumptions stated in section 1, matrices $\underline{\underline{A}}_1$ and $\underline{\underline{G}}$, material properties $\underline{\underline{\mathcal{D}}}^{(i)+}$, and the integration domains all remain constant along the beam's span, and hence, matrices $\underline{\underline{M}}^{(i)}$, $\underline{\underline{C}}^{(i)}$, and $\underline{\underline{E}}^{(i)}$ are constant as well.

3.2 Assembly of panel's stiffnesses

The strain energy of the complete system is simply the sum of those of the m panels of the beam. Consider two neighboring panels, defined by curves $\Gamma^{(i-1)}$ and $\Gamma^{(i)}$, and sharing a common node at point **Q**, as depicted in fig. 2. At point **Q**, the displacements and rotations are unique but their components in the local bases for panels $i-1$ and i are denoted $\underline{\mathbf{u}}_Q^{(i-1)+}$ and $\underline{\mathbf{u}}_Q^{(i)+}$, respectively. Let rotation matrices $\underline{\underline{R}}_r^{(i-1)}$ and $\underline{\underline{R}}_r^{(i)}$ denote the rotations that bring sectional basis $\mathcal{B}^* = (\bar{b}_1, \bar{b}_2, \bar{b}_3)$ to the local bases $\mathcal{B}^{(i-1)} = (\bar{b}_1, \bar{t}^{(i-1)}, \bar{n}^{(i-1)})$ and $\mathcal{B}^{(i)} = (\bar{b}_1, \bar{t}^{(i)}, \bar{n}^{(i)})$ for these panels, *i.e.*,

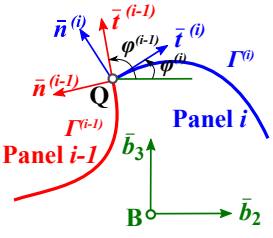

Figure 2: Two adjacent panels.

$$\underline{\underline{R}}_r^{(i-1)} = \begin{bmatrix} 1 & 0 & 0 \\ 0 & \cos\phi^{(i-1)} & -\sin\phi^{(i-1)} \\ 0 & \sin\phi^{(i-1)} & \cos\phi^{(i-1)} \end{bmatrix}, \tag{7a}$$

$$\underline{\underline{R}}_r^{(i)} = \begin{bmatrix} 1 & 0 & 0 \\ 0 & \cos\phi^{(i)} & -\sin\phi^{(i)} \\ 0 & \sin\phi^{(i)} & \cos\phi^{(i)} \end{bmatrix}, \tag{7b}$$

where where $\phi^{(i-1)}$ and $\phi^{(i)}$ are the magnitudes of rotation that takes place about unit vector $\bar{b}_i$. The following compatibility condition must hold: $\underline{\underline{\mathfrak{R}}}^{(i-1)}\underline{\mathfrak{u}}_Q^{(i-1)+} = \underline{\underline{\mathfrak{R}}}^{(i)}\underline{\mathfrak{u}}_Q^{(i)+}$, where $\underline{\underline{\mathfrak{R}}}^{(i-1)} = \text{diag}(\underline{\underline{R}}_r^{(i-1)}, \underline{\underline{R}}_r^{(i-1)})$ and $\underline{\underline{\mathfrak{R}}}^{(i)} = \text{diag}(\underline{\underline{R}}_r^{(i)}, \underline{\underline{R}}_r^{(i)})$.

The beam's strain energy is now $L = \sum_{i=1}^{m} L^{(i)}$. Because the normal vectors of two adjacent panels differ, the junction nodes possess six degrees of freedom. Using the compatibility conditions, the panels' stiffness matrices, $\underline{\underline{M}}^{(i)}$, $\underline{\underline{C}}^{(i)}$, and $\underline{\underline{E}}^{(i)}$ can be assembled into their global counterparts, denoted $\underline{\underline{M}}$, $\underline{\underline{C}}$, and $\underline{\underline{E}}$, respectively, and the array storing the combined displacements at all the nodes is denoted $\hat{\underline{\mathfrak{u}}}$. If each of the m connected panels are discretized with $\ell^{(i)}$ nodes, the total number of degree of freedom is $n = \sum_{i=1}^{m} 5\ell^{(i)} - 4k_2 - 9k_3 - 14k_4 \ldots$, where k_2, k_3, and k_4 are the numbers of junction nodes where two, three, and four panels intersect, respectively. Finally, the beam's strain energy density becomes

$$L = \frac{1}{2}\sum_{i=1}^{m}\left[\hat{\underline{\mathfrak{u}}}'\left(\underline{\underline{M}}\,\hat{\underline{\mathfrak{u}}}' + \underline{\underline{C}}^T\hat{\underline{\mathfrak{u}}}\right) + \hat{\underline{\mathfrak{u}}}^T\left(\underline{\underline{C}}\,\hat{\underline{\mathfrak{u}}}' + \underline{\underline{E}}\,\hat{\underline{\mathfrak{u}}}\right)\right]. \tag{8}$$

3.3 Governing equations

The array of stress resultants acting at the nodes of the i^{th} panel is defined as $\hat{\underline{\mathfrak{p}}}^{(i)} = \int_{\Gamma^{(i)}} \underline{\underline{N}}^T \underline{\mathfrak{f}}_1^+ \, \mathrm{d}\alpha_2^{(i)}$, where array $\underline{\mathfrak{f}}_1^+ = \underline{\underline{A}}_1^T \underline{\mathfrak{f}}^+$ stores the stress resultants acting on face of the i^{th} panel, normal to unit vector $\bar{b}_1$. Introducing the material constitutive laws $\underline{\mathfrak{f}}^+ = \underline{\underline{\mathcal{D}}}^+ \underline{\mathfrak{e}}^+$ and the sectional strains given by eq. (3) yields $\hat{\underline{\mathfrak{p}}}^{(i)} = \underline{\underline{M}}^{(i)}\,\hat{\underline{\mathfrak{u}}}^{(i)\prime} + \underline{\underline{C}}^{(i)T}\hat{\underline{\mathfrak{u}}}^{(i)}$. Assembling all the panels then leads to

$$\hat{\underline{\mathfrak{p}}} = \underline{\underline{M}}\,\hat{\underline{\mathfrak{u}}}' + \underline{\underline{C}}^T\hat{\underline{\mathfrak{u}}}. \tag{9}$$

where array $\hat{\underline{\mathfrak{p}}}$ stores the stress resultants, $\hat{\underline{\mathfrak{p}}}^{(i)}$, of all panels.

For this problem, the strain energy density is also the Lagrangian of the system. Because the nodal forces defined by eq. (9) can be written as $\hat{\underline{\mathfrak{p}}} = \partial L/\partial\hat{\underline{\mathfrak{u}}}'$, the nodal displacements and forces are dual variables in Hamilton's formalism. The Hamiltonian of the system, denoted H, is defined via Legendre's transformation [27] as $H = \hat{\underline{\mathfrak{p}}}^T\hat{\underline{\mathfrak{u}}}' - L$ and tedious algebra reveals that $H = -1/2\ \hat{\underline{\mathcal{X}}}^T(\underline{\underline{\mathcal{J}}}\,\underline{\underline{\mathcal{H}}})\hat{\underline{\mathcal{X}}}$, where array $\hat{\underline{\mathcal{X}}}$ stores the nodal displacements and forces $\hat{\underline{\mathcal{X}}}^T = \{\hat{\underline{\mathfrak{u}}}^T\ \hat{\underline{\mathfrak{p}}}^T\}$, and matrix $\underline{\underline{\mathcal{H}}}$, of size $2n \times 2n$, is defined as

$$\underline{\underline{\mathcal{H}}} = \begin{bmatrix} -\underline{\underline{M}}^{-1}\underline{\underline{C}}^T & \underline{\underline{M}}^{-1} \\ \underline{\underline{E}} - \underline{\underline{C}}\,\underline{\underline{M}}^{-1}\underline{\underline{C}}^T & \underline{\underline{C}}\,\underline{\underline{M}}^{-1} \end{bmatrix}. \tag{10}$$

Matrix $\underline{\underline{\mathcal{J}}}$ is defined in B and matrix $\underline{\underline{\mathcal{H}}}$ is a constant Hamiltonian matrix, see definition (20).

Hamilton's canonical equations are

$$\hat{\underline{\mathcal{X}}}' = \underline{\underline{\mathcal{J}}}\,\frac{\partial H}{\partial\hat{\underline{\mathcal{X}}}} = \underline{\underline{\mathcal{H}}}\,\hat{\underline{\mathcal{X}}}, \tag{11}$$

where identity $\underline{\underline{\mathcal{J}}}\,\underline{\underline{\mathcal{J}}} = -\underline{\underline{I}}$ is used. Equation (11) is composed of two sets of n first-order, linear ordinary differential equations. The first set, $\hat{\underline{\mathfrak{u}}}' = \partial H/\partial\hat{\underline{\mathfrak{p}}}$, is identical to eqs. (9) and provides the constitutive relation between nodal forces and nodal displacements. The second set, $\hat{\underline{\mathfrak{p}}}' = -\partial H/\partial\hat{\underline{\mathfrak{u}}}$, defines the nodal equilibrium equations.

4 Algebraic structure of the solutions

Clearly, thin-walled beam problems can be represented by linear, homogeneous Hamiltonian systems. The nature of the solutions depends on the eigenvalues of the system matrix, Hamiltonian

matrix $\underline{\underline{\mathcal{H}}}$. Similar as the problem of beams with solid-sections [23], matrix $\underline{\underline{\mathcal{H}}}$ can be reduced to the following uncoupled form under a symplectic transformation

$$\underline{\underline{\mathcal{H}}} \sim \operatorname{diag}\left(\begin{bmatrix} -\tilde{\mathcal{K}}^* & \underline{\underline{\mathcal{S}}}^* \\ \underline{\underline{0}} & \tilde{\mathcal{K}}^{*T} \end{bmatrix}, \begin{bmatrix} +\lambda_1 & & \\ & +\lambda_2 & \\ & & \ddots \end{bmatrix}, \begin{bmatrix} -\lambda_1 & & \\ & -\lambda_2 & \\ & & \ddots \end{bmatrix}\right), \tag{12}$$

where $\tilde{\mathcal{K}}^*$ is defined as

$$\tilde{\mathcal{K}}^* = \begin{bmatrix} 0 & 0 & 0 & 0 & 0 & 0 \\ 0 & 0 & 0 & 0 & 0 & -1 \\ 0 & 0 & 0 & 0 & 1 & 0 \\ 0 & 0 & 0 & 0 & 0 & 0 \\ 0 & 0 & 0 & 0 & 0 & 0 \\ 0 & 0 & 0 & 0 & 0 & 0 \end{bmatrix}, \tag{13}$$

matrix $\underline{\underline{S}}^*$, of size 6×6, stores the beam's sectional compliance components resolved in the sectional basis [23], and $\pm\lambda_i$ are the i^{th} pairs of non-vanishing eigenvalues of matrix $\underline{\underline{\mathcal{H}}}$. The predicted sectional compliance takes into account warping deformations.

In eq. (12), the first block, of size 12×12, corresponds to the null eigenvalues of the Hamiltonian and gives rise to polynomial solutions, or the solution of Saint-Venant's problem. These solutions have been called the "central solutions" by Giavotto *et al.* [19] or "center manifold" by Mielke [21]. The second and third blocks in eq. (12) store the non-vanishing eigenvalues of matrix $\underline{\underline{\mathcal{H}}}$ and give rise to exponentially decaying solutions. These solutions have been called the "extremity solutions" by Giavotto *et al.* [19].

The symplectic transformation matrix is composed of three parts [23]

$$\underline{\underline{S}}_c = \begin{bmatrix} \underline{\underline{Z}} & \underline{\underline{W}} \\ \underline{\underline{0}} & \underline{\underline{Y}} \end{bmatrix}, \ \underline{\underline{S}}_{e+} = \begin{bmatrix} \underline{U}_{1+} & \underline{U}_{2+} & \cdots \\ \underline{V}_{1+} & \underline{U}_{2+} & \cdots \end{bmatrix}, \ \underline{\underline{S}}_{e-} = \begin{bmatrix} \underline{U}_{1-} & \underline{U}_{2-} & \cdots \\ \underline{V}_{1-} & \underline{U}_{2-} & \cdots \end{bmatrix}, \tag{14}$$

where matrix $\underline{\underline{Z}}$, of size n×6, stores the nodal displacements due to the rigid-section motion; matrices $\underline{\underline{W}}$ and $\underline{\underline{Y}}$, both of size $n \times 6$, stores the nodal warping and forces induced by unit sectional stress resultants, respectively; matrices $\underline{\underline{U}}_{\pm}$ and $\underline{\underline{V}}_{\pm}$, both or size $n \times k$, store the k pairs of eigenvectors associated with non-vanishing eigenvalues of the Hamiltonian matrix. In summary, the first 12 columns of matrix $\underline{\underline{\mathcal{S}}}_c$ span the eigensubspace of Hamiltonian matrix, $\underline{\underline{\mathcal{H}}}$, associated with its null eigenvalues; while the $2k$ columns of matrices $\underline{\underline{\mathcal{S}}}_{e+}$ and $\underline{\underline{\mathcal{S}}}_{e-}$ span the eigensubspace associated with those $2k$ non-vaninsing eigenvalues.

For straight beams subjected to loads and displacement constraints at the end sections, closed-form central and extremity solutions have been found by the authors [23]. Suppose that the first k pairs of extremity modes are considered and denote $\underline{\underline{\Lambda}} = \operatorname{diag}(\lambda^{(j)})$, $j = 1, 2, \ldots, k$. The complete solution is a combination of central solutions and extremity solutions

$$\underline{\hat{\mathcal{X}}}(\alpha_1) = \underline{\underline{\mathcal{S}}}_c \underline{\underline{\mathcal{G}}}_c(\alpha_1)\underline{\mathcal{L}}_{c0} + \underline{\underline{\mathcal{S}}}_{e+} \exp\left((\alpha_1 - L)\underline{\underline{\Lambda}}\right) \underline{\mathfrak{a}}_{L+} + \underline{\underline{\mathcal{S}}}_{e-} \exp\left(-\alpha_1 \underline{\underline{\Lambda}}\right) \underline{\mathfrak{a}}_{0-}, \tag{15}$$

where $\underline{\mathcal{L}}_{c0}^T = \{\underline{\mathcal{U}}_0^{*T} \ \underline{\mathcal{F}}_0^{*T}\}$, stores the the 6 average rigid-section motions, $\underline{\mathcal{U}}_0^*$, and 6 stress resultants, $\underline{\mathcal{F}}_0^*$, at the beam's tip ($\alpha_1 = 0$), respectively; arrays $\underline{\mathfrak{a}}_{+L}$ and $\underline{\mathfrak{a}}_{-0}$, both of size $k \times 1$, store the magnitudes of extremity modes at the beam's tips, $\alpha_1 = L$ and $\alpha_1 = 0$, respectively; matrix function $\underline{\underline{\mathcal{G}}}_c$ is given in C. For convenience, eq. (15) are rewritten as

$$\underline{\hat{\mathfrak{u}}} = \underline{\underline{\mathcal{U}}}\,\underline{\underline{\mathcal{G}}}(\alpha_1)\underline{\mathcal{L}}, \tag{16a}$$

$$\underline{\hat{\mathfrak{p}}} = \underline{\underline{\mathcal{P}}}\,\underline{\underline{\mathcal{G}}}(\alpha_1)\underline{\mathcal{L}}, \tag{16b}$$

where $\underline{\underline{\mathcal{U}}} = [\underline{\underline{Z}} \;\; \underline{\underline{W}} \;\; \underline{\underline{U}}_+ \;\; \underline{\underline{U}}_-]$ and $\underline{\underline{\mathcal{P}}} = [\underline{\underline{0}} \;\; \underline{\underline{Y}} \;\; \underline{\underline{V}}_+ \;\; \underline{\underline{V}}_-]$, $\underline{\mathcal{L}}^T = \{\underline{\mathcal{L}}_{c0}^T, \underline{\mathfrak{a}}_{+L}^T, \underline{\mathfrak{a}}_{-0}^T\}$, and $\underline{\underline{\mathcal{G}}}(\alpha_1) = \text{diag}\left(\underline{\underline{\mathcal{G}}}_c(\alpha_1), \exp((\alpha_1 - L)\underline{\underline{\Lambda}}), \exp(-\alpha_1\underline{\underline{\Lambda}})\right)$.

Clearly, extremity solutions are decaying exponentially from the beam's ends. For beams with solid cross-sections, the longest decay lengths are roughly equal to the representative dimension of the cross-section and hence, the extremity solutions affect a small region near the beam's ends only [25, 28]. For thin-walled beams, the longest decay length are much larger, sometimes of the order of the beam's length. Consequently, the extremity solutions affect the entire span of the beam and must be taken into account if accurate solutions are to be found.

5 Boundary conditions

The only indeterminacy remaining in the complete solution (16) of the problem are the boundary values, $\underline{\mathcal{L}}$. A weak form of the two-dimensional boundary conditions at the beam's two ends will be enforced,

$$\left[\delta\hat{\underline{\mathfrak{u}}}^T(\hat{\underline{\mathfrak{p}}}_b - \hat{\underline{\mathfrak{p}}}) - \delta\hat{\underline{\mathfrak{p}}}^T(\hat{\underline{\mathfrak{u}}}_b - \hat{\underline{\mathfrak{u}}})\right]_0 = 0, \tag{17a}$$

$$\left[\delta\hat{\underline{\mathfrak{u}}}^T(\hat{\underline{\mathfrak{p}}}_b - \hat{\underline{\mathfrak{p}}}) - \delta\hat{\underline{\mathfrak{p}}}^T(\hat{\underline{\mathfrak{u}}}_b - \hat{\underline{\mathfrak{u}}})\right]_L = 0, \tag{17b}$$

where $\hat{\underline{\mathfrak{u}}}_b$ and $\hat{\underline{\mathfrak{p}}}_b$ are the prescribed nodal displacements and forces, respectively, at the beam's ends. Three types of boundary conditions are commonly encountered: *(1)* nodal displacements are prescribed over contour Γ, *(2)* nodal forces are prescribed over the same contour, or *(3)* nodal displacements and forces are prescribed over mutually exclusive portions of the contour.

To illustrate the process, it is assumed that the nodal displacements are specified at the beam's ends, $\hat{\underline{\mathfrak{u}}}(0) = \hat{\underline{\mathfrak{u}}}_0$, and $\hat{\underline{\mathfrak{u}}}(L) = \hat{\underline{\mathfrak{u}}}_L$. Other types of boundary conditions can be derived easily in a similar manner. Introducing the specified values into eq. (17), and noting that variations $\delta\hat{\underline{\mathfrak{u}}}_0$ and $\delta\hat{\underline{\mathfrak{u}}}_L$ vanish yields $\delta\hat{\underline{\mathfrak{p}}}(0)^T[\hat{\underline{\mathfrak{u}}}_0 - \hat{\underline{\mathfrak{u}}}(0)] = 0$ and $\delta\hat{\underline{\mathfrak{p}}}(L)^T[\hat{\underline{\mathfrak{u}}}_L - \hat{\underline{\mathfrak{u}}}(L)] = 0$. Introducing closed-form solutions (16) then leads to

$$\delta\underline{\mathcal{L}}^T\left(\begin{bmatrix}\underline{\underline{\mathcal{A}}}_0\\ \underline{\underline{\mathcal{A}}}_L\end{bmatrix}\underline{\mathcal{L}} - \begin{Bmatrix}\underline{\mathfrak{b}}_0\\ \underline{\mathfrak{b}}_L\end{Bmatrix}\right) = 0, \tag{18}$$

where matrices $\underline{\underline{\mathcal{A}}}_0 = \underline{\underline{\mathcal{G}}}(0)^T\underline{\underline{\mathcal{P}}}^T\underline{\underline{\mathcal{U}}}\,\underline{\underline{\mathcal{G}}}(0)$ and $\underline{\underline{\mathcal{A}}}_L = \underline{\underline{\mathcal{G}}}(L)^T\underline{\underline{\mathcal{P}}}^T\underline{\underline{\mathcal{U}}}\,\underline{\underline{\mathcal{G}}}(L)$ are both of size $(12{+}2k)\times(12{+}2k)$ and array $\underline{\mathfrak{b}}_0 = \underline{\underline{\mathcal{G}}}(0)^T\underline{\underline{\mathcal{P}}}^T\,\hat{\underline{\mathfrak{u}}}_0$, $\underline{\mathfrak{b}}_L = \underline{\underline{\mathcal{G}}}(L)^T\underline{\underline{\mathcal{P}}}^T\,\hat{\underline{\mathfrak{u}}}_L$. The enforcement of boundary conditions (18) leads to a set of over-determined equations for the unknowns, $\underline{\mathcal{L}}$; a least squares solution is found easily.

6 Numerical examples

To validate the proposed approach, a set of numerical examples will be presented. For all examples presented here, the panels' through-the-thickness geometric and material properties were used to compute their stiffness matrices using the procedure developed by Han and Bauchau [29]. The warping and stress resultants distributions associated with non-vanishing eigenvalues are normalized by the norm of nodal displacements and nodal forces, $\|\hat{\underline{\mathfrak{u}}}\|$, and $\|\hat{\underline{\mathfrak{p}}}\|$, respectively.

6.1 I-beam

Figure 3 depicts a straight cantilevered I-beam of length $L = 5.0$ m. The two flanges are of width $2b = 0.6$ m and thickness $t_f = 0.02$ m; the web is of height $2h = 1.2$ m and thickness $t_w = 0.01$ m. The beam is subjected to a tip eccentric transverse force, $\underline{P} = -1\bar{\imath}_3$ kN. The beam is made of an

isotropic material with Young's modulus $E = 210$ GPa and Poisson's ratio $\nu = 0.3$. In the present approach, meshes of 16 and 32 3-node one-dimensional elements were used to discretize each flange and the web, respectively.

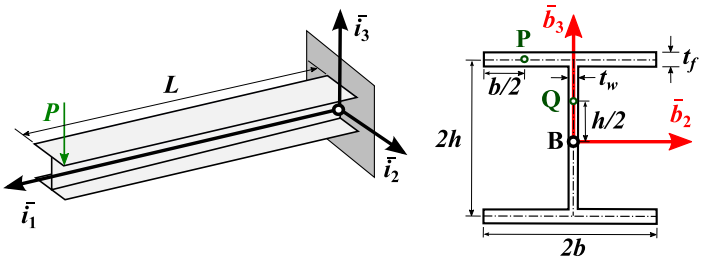

Figure 3: Configuration of the I-beam

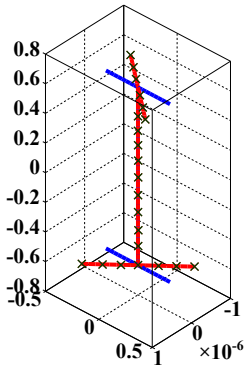

Figure 4: Warping due to a unit torque: present (solid line), Vlasov: (×).

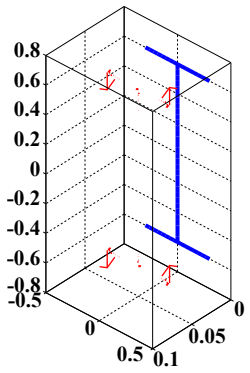

Figure 5: Resultant forces due to a unit torque.

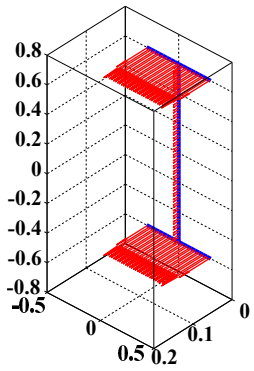

Figure 6: Resultant moments due to a unit torque.

The out-of-plane warping generated by a unit torque is shown in fig. 4. The present predictions coincides with those obtained by using Vlasov's theory [3]. The distributions of resultant force and moment components, $\underline{n}_1$ and $\underline{m}_1$, due to a unit torque are shown in figs. 5 and 6, respectively; for clarity, the resultant forces are plotted in a plane parallel to that of the cross-section. The transverse shear force and twisting moment are the only non-vanishing components under torque and each of them contribute to half of the torque. This is consistent with the analytical solutions of Reissner plates under pure torsion [30, 31]. The distribution of shear forces converge to six corner forces, four at the tip of the flanges and two at the junctions of the flanges with the web.

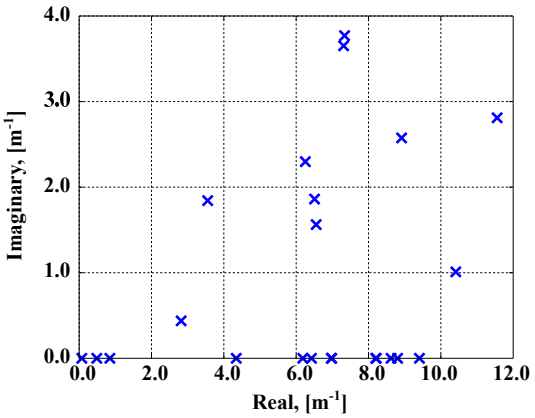

Figure 7: The lowest 21 eigenvalues with a non-vanishing real part.

Fig. 7 shows the lowest 21 eigenvalues presenting non-vanishing real parts. Because the eigenvalues of Hamiltonian matrices are of the form $\pm\sigma \pm i\omega$, the figure only shows the eigenvalues with positive real and imaginary parts. The magnitudes of the first three pairs of eigenvales are much smaller than those of others. In Vlasov's beam theory [3], the decay rate of the primary warping mode is found to be $d = \sqrt{GJ/EI_\omega} = 0.0731$ m^{-1}, where GJ and EI_ω are Saint-Venant's torsional stiffness and Vlasov's warping stiffness, respectively. In the present approach, the magnitude of the lowest pair of eigenvalues is 0.0727 m^{-1}; the small discrepancy results from the assumptions inherent to Vlasov's theory.

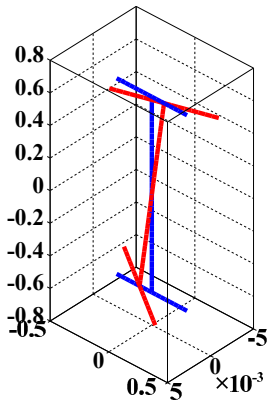

Figure 8: Warping associated with λ_1.

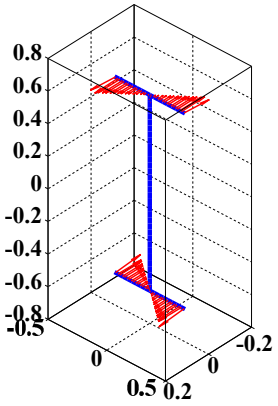

Figure 9: Resultant forces associated with λ_1.

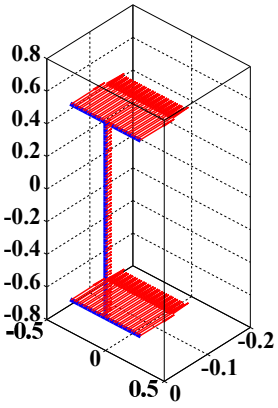

Figure 10: Resultant moments associated with λ_1.

Figure 8 depicts the warping distribution associated with the lowest positive eigenvalue, λ_1: besides out-of-plane warping, the section undergoes in-plane rotation. Figures 9 and 10 show the corresponding internal force and moment components, $\underline{n}_1$ and $\underline{m}_1$, respectively. The distributions associated with the negative eigenvalue, $-\lambda_1$ have identical shapes, but some components are of the opposite sign. Figure 9 shows that axial forces distributed along the top and bottom flanges generate two bending moments of opposite sign. In Vlasov's theory, they are called the "bi-moments." Twisting moments (shown in fig. 10) also appear in the flanges and web; these are neglected in Vlasov's theory. The magnitudes of the second and third pairs of eigenvalues are 0.487 m^{-1} and 0.849 m^{-1}, respectively. These two extremity solutions exhibit both in-plane and out-of-plane warping and play an important role in the present problem because tip sections undergo large in-plane distortion under the eccentric load.

To validate the predictions of the proposed approach, a two-dimensional FEM analysis was performed using ABAQUS with a mesh of 64×128 8-node quadrilateral S8R6 shell elements. The solution of Vlasov's theory [3] is also presented for reference. Figure 11 contrasts the deformed configurations of the beam for the three models. As depicted in fig. 11b, Vlasov's theory does not predict in-plane distortion and hence, does not yield accurate predictions for the present problem. When the first three pairs of dominant extremity solutions are taken into account, the present approach gives reasonable predictions, as shown in fig. 11c.

Next, the torsion angle, θ_1, and the axial force per unit length along the sectional contour, N_{11}, at points **P** and **Q** indicated in fig. 3 were evaluated along the beam's span. Figures 12a and 12b show these quantities at the flange's mid-plane point **P** whereas the corresponding quantities at the web's mid-plane point **Q** are shown in figs. 13a and 13b. Clearly, Vlasov's theory does not yield accurate predictions along the beam's span. In fact, Vlasov's predictions are equivalent to those of the present approach when using the first pair of extremity modes only. Better predictions are obtained when the present approach includes the lowest three pairs of extremity solutions. The remaining extremity solutions affect the response near the beam's ends only. Trial and error reveal that 32 extremity modes only contribute to the response significantly. With the inclusion of these

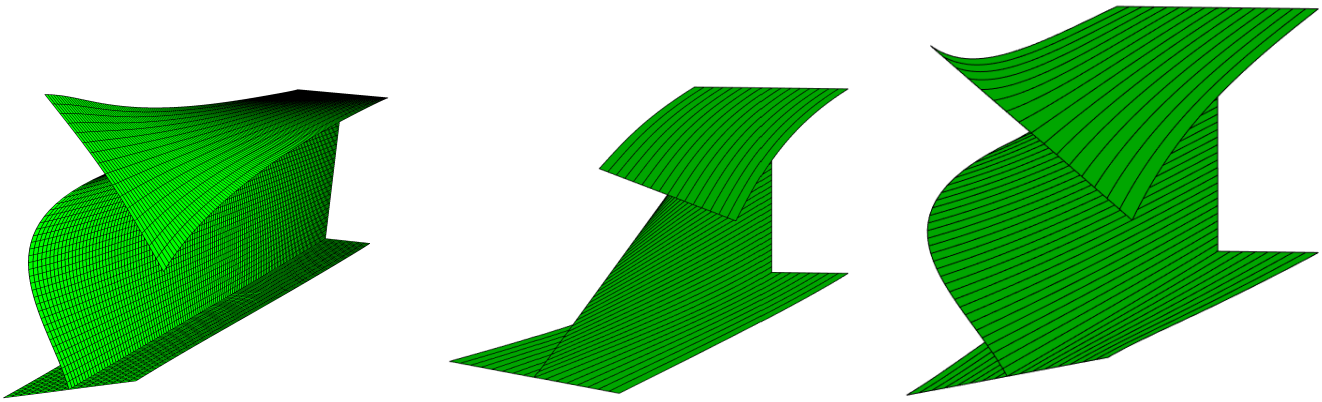

(a) ABAQUS model (b) Vlasov model (c) Present model, $2n_e = 6$

Figure 11: Deformed configurations of the I beam.

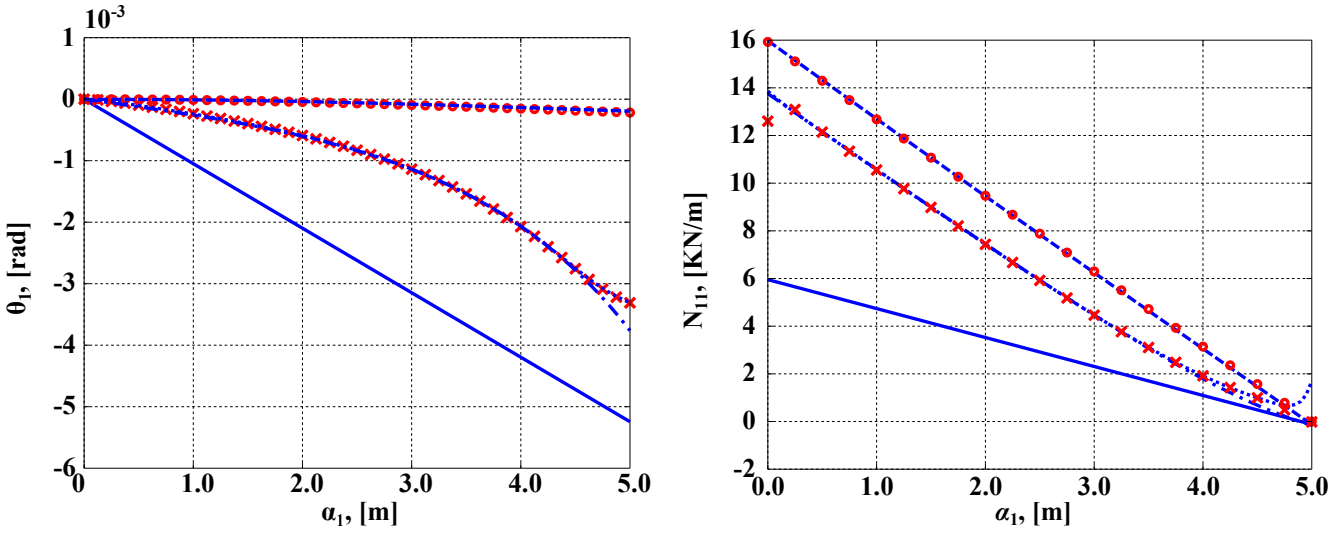

(a) Torsion angle, θ_1 (b) Axial force per unit span, N_{11}

Figure 12: Torsion angle and axial force at point **P**, Vlasov: $\circ$, ABAQUS: $\times$, present: solid line ($2n_e = 0$), dashed line ($2n_e = 2$), dashed-dotted line ($2n_e = 6$), dotted line ($2n_e = 32$).

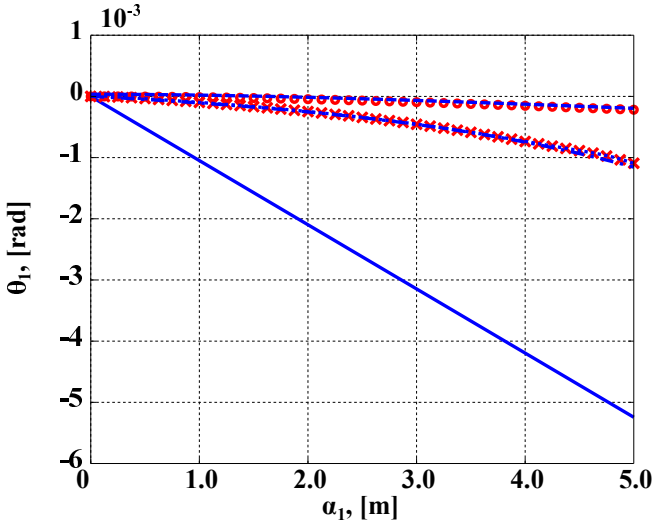

(a) Torsion angle, θ_1

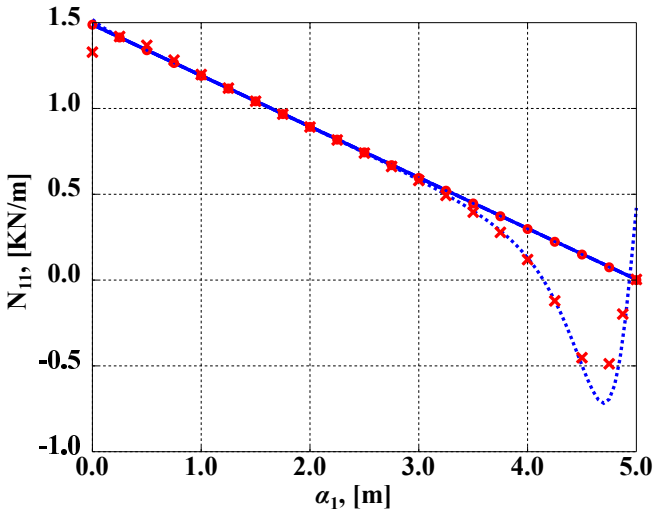

(b) Axial force per unit arch-length, N_{11}

Figure 13: Torsion angle and axial force at point **Q**, Vlasov: ∘, ABAQUS: ×, present: solid line ($2n_e = 0$), dashed line ($2n_e = 2$), dashed-dotted line ($2n_e = 6$), dotted line ($2n_e = 32$).

32 dominant modes, the present predictions are in excellent agreement with those of the shell FEM model.

6.2 Hollow-flange channel

Figure 14 depicts a straight cantilevered beam of length $L = 1.0$ m. The two hollow flanges are of width $b = 0.06$ m and height $t_f = 0.015$ m; the web is of height $2h = 0.17$ m and all the walls are of thickness $t_w = 0.0016$ m. The beam is subjected to a tip eccentric transverse force, $\underline{P} = -5\bar{\imath}_3$ kN, as depicted in fig. 14. The beam is made of an isotropic material with Young's modulus $E = 210$ GPa and Poisson's ratio $\nu = 0.3$. This example has been investigated by Vieira *et al.* [32] using the Generalized Beam Theory, which ignores the effects of transverse shear deformation of the walls.

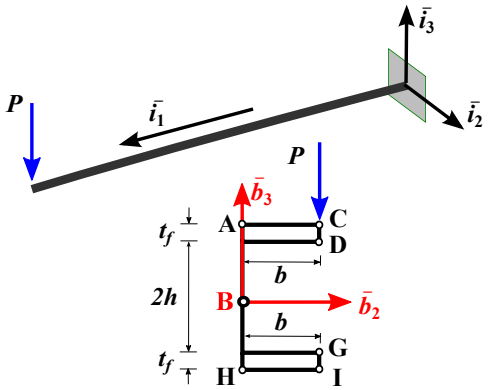

Figure 14: Configuration of the C channel with hollow-flanges.

In the present approach, meshes of 8 and 6 3-node one-dimensional elements were used to discretize each flange and the web, respectively. The diagonal terms of the beam's 6×6 sectional stiffness matrix predicted by the present approach are $S^*_{11} = 157.92$ MN (extension), $S^*_{22} = 16.36$ MN (shear along $\bar{b}_2$), $S^*_{33} = 23.03$ MN (shear along $\bar{b}_2$), $S^*_{44} = 200$ KN·m^2 (torsion), $S^*_{55} = 100$ KN·m^2 (bending along $\bar{b}_2$), and $S^*_{66} = 130$ KN·m^2 (bending along $\bar{b}_3$). Because the cross-section is not symmetric, two off-diagonal terms appear, $S^*_{34} = 570$ KN·m (shear-twisting coupling) and $S^*_{16} = -3.02$ MN·m (stretching-bending coupling).

The distributions of the axial force component, N_{11}, at the six corners **A**, **C**, **D**, **G**, **H** and **I** are shown in figs. 15 and 16, for the present approach with $2n_e = 28$ and ABAQUS, respectively. For reference, the solutions obtained by Vieira *et al.* [32], using about the same number of deformation modes are also presented. Good correlations are observed for all the three types of solutions.

The computational cost of the proposed and Vieira's approaches are nearly identical because

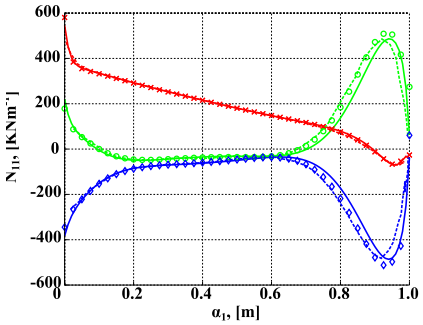

Figure 15: Axial force per unit arch-length, N_{11}, present solution: solid line, Vieira: dashed line; ABAQUS: $\times$(**A**), $\circ$(**B**), $\diamond$(**G**).

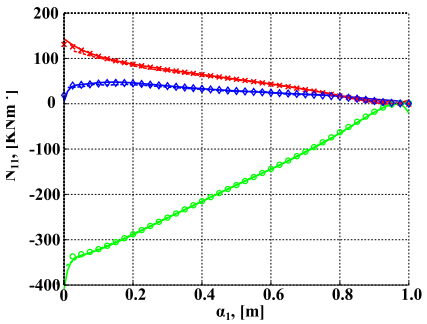

Figure 16: Axial force per unit arch-length, N_{11}, present solution: solid line, Vieira: dashed line; ABAQUS: $\times$(**G**), $\circ$(**I**), $\diamond$(**H**).

both methods involve a sectional analysis followed by a one-dimensional beam analysis. The proposed approach presents the following advantages: *(1)* it can handle curved sectional geometries, *(2)* transverse shear deformation of the strips is taken into account, *(*3*)* the beam's 6×6 sectional stiffness matrix is a by-product of the analysis; it takes into account warping effects, *(4)* for beams loaded at their ends only, closed-form solutions have been presented.

6.3 Composite thin-walled section beam

Figure 17 depicts a thin-walled cantilevered beam of length $L = 0.5$ m with a cross-section consisting of two half-circles of radius $\rho = 50$ mm, connected at points **C** and **D**. The beam's tip cross-section remains rigid and its motion is prescribed as follows: reference point **B** translates of $u_3 = 0.1$ mm along unit vector $\bar{b}_3$ and the plane of the section rotates by $\theta_1 = 0.1$ mrad about unit vector $\bar{b}_1$. The thin walls consist of four plies of graphite/epoxy material with the following properties: ply thickness $t_p = 1.25$ mm, longitudinal modulus $E_L = 25.0$ MPa, transverse modulus $E_T = 1.0$ MPa, shearing modulus $G_{LT} = 0.5$ MPa, and Poisson's ratios $\nu_{LT} = 0.25$, $\nu_{TN} = 0.25$. The lay-up configuration presents the following stacking sequence, starting from the inner ply, $[0°; 90°_2; 0°]$; 0° fibers are aligned with unit vector $\bar{b}_1$ and a positive ply angle indicates a right-hand rotation about outer normal vector $\bar{n}$, as depicted in fig. 17. The sign conventions for internal force components on the right-hand side panel, N_{11}^+ and N_{12}^+, are also illustrated in fig. 17.

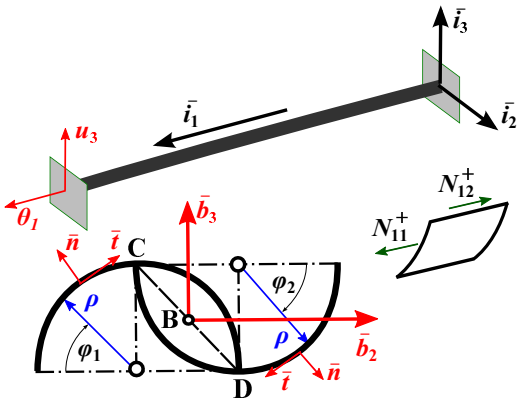

Figure 17: Configuration of the composite thin-walled beam

For reference, a two-dimensional FEM analysis was performed using S8R6 shell elements in ABAQUS. The meshes used in the two approaches and the associated computational costs are listed in table 1. In both cases, the main cost is the factorization of the stiffness matrix, which can be estimated [33] as $\mathcal{C} \propto nm^2$, where n is the size of the stiffness matrix and m its average half-bandwidth. For the present approach, the extremity solutions must be evaluated by solving an eigenvalue problem at an extra cost. In this work, Arnoldi's algorithm was used to solve the eigenproblem; the cost of this step is estimated as $nm^2 + knm$, where k is the number of Arnoldi steps. The proposed approach consists a sectional analysis and beam analysis. Because the beam is loaded at its end sections only, analytical solutions along the beam's span can be used directly, see eq. (16); alternatively; a beam finite element analysis can be used for this step. As expected,

the proposed approach is several orders of magnitude more efficient than shell FEM analysis, see table 1.

Table 1: Estimation of computational cost.

	Proposed		ABAQUS
	Sectional analysis	1D analysis	
Mesh	34, 3 node 1D	Analytical or 6, 4 node 1D	64×56, 8-node 2D
Cost	$640 \times 15^2 +$ $60 \times 640 \times 15$	Negligible or 120×24^2	$54,000 \times 1,500^2$

The diagonal terms of the beam's 6×6 sectional stiffness matrix predicted by the present approach are $S^*_{11} = 20.5$ kN, $S^*_{22} = 0.372$ kN, $S^*_{33} = 0.347$ kN, $S^*_{44} = 0.136$ N·m^2, $S^*_{55} = 5.86$ N·m^2, and $S^*_{66} = 0.385$ N·m^2. Because the cross-section is not symmetric, two off-diagonal terms appear, $S^*_{23} = 1.96$ N (shear coupling along unit vectors $\bar{b}_2$ and $\bar{b}_3$) and $S^*_{56} = 3.52$ N·m^2 (bending coupling about unit vectors $\bar{b}_2$ and $\bar{b}_3$).

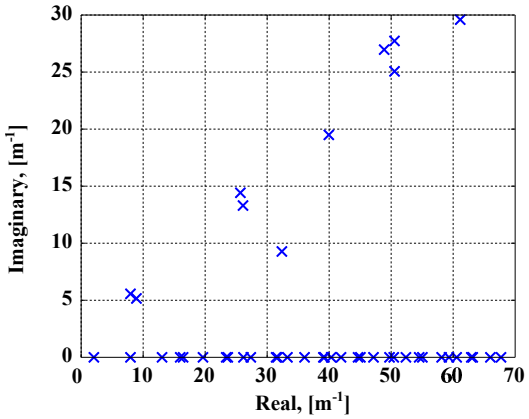

Figure 18: The lowest 21 eigenvalues with a non-vanishing real part.

Fig. 18 shows the lowest 41 eigenvalues presenting non-vanishing real parts. The lowest eigenvalue has a magnitude of 2.0524 m^{-1}. Specific displacement and force components were evaluated along the beam's span at point **P**, located at $\varphi_1 = 0.785\pi$, as shown in fig. 17. With the inclusion of the first pair of extremity modes, the present predictions for displacement are in excellent agreement with the shell FEM results, as shown in fig. 19. The extremity solutions do affect the rotation components near the beam's two ends. Trial and error revealed that 22 extremity modes only made contribute to the response only. Predictions including the 22 dominant modes were found to be in excellent agreement with ABAQUS predictions, as shown in fig. 20.

The distributions of the axial force component, N^+_{11}, over the mid-plane surface of the right-hand side panel are shown in figs. 21 and 22, for the present approach with $n_e = 0$ (Saint-Venant's solution) and ABAQUS, respectively. The effects of extremity solutions are negligible, as shown in fig. 21 and 22. Accurate predictions are obtained using the central solutions only.

On the other hand, the extremity solutions do affect other shear forces. The distributions of the in-plane shear force component, N^+_{12}, over the mid-plane surface of the right-hand side panel are shown in figs. 23, 24, and 25, for the present approach with $n_e = 0$ (Saint-Venant's solution), using the 22 dominant modes, and ABAQUS, respectively. The extremity solutions affect the distribution significantly near the two ends, as shown in fig. 23 and 24. Accurate predictions are obtained only when taking into account the dominant extremity solutions.

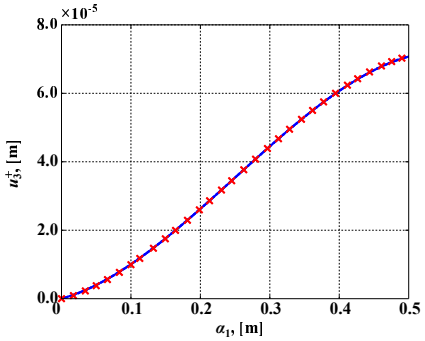

Figure 19: Transverse displacement component, u_3^+, at point **P**, ABAQUS: $\times$, present: solid line $2n_e = 0$, dotted line: $2n_e = 2$.

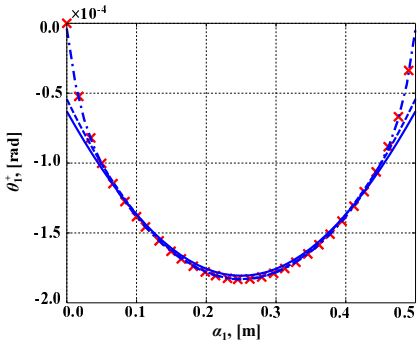

Figure 20: Rotation component, θ_1^+, at point **P**, ABAQUS: $\times$, present: solid line $2n_e = 0$, dotted line: $2n_e = 2$, dashed-dotted line: $2n_e = 22$.

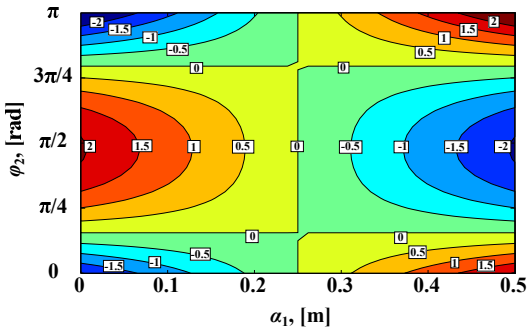

Figure 21: Resultant axial force component, N_{11}^+ ($\mathrm{N{\cdot}m^{-1}}$), present solution, $n_e = 0$.

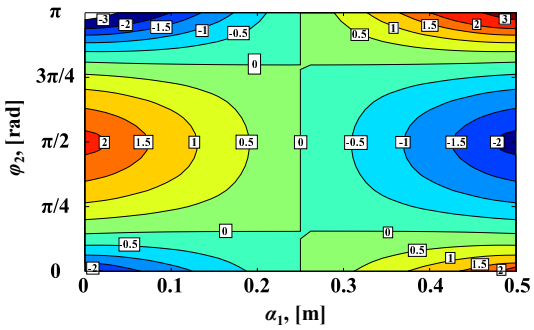

Figure 22: Resultant axial force component, N_{11}^+ ($\mathrm{N{\cdot}m^{-1}}$), ABAQUS.

7 Conclusions

This paper has extended the Hamiltonian approach to the analysis of thin-walled beams. For beams consisting of thin panels, the governing equations are cast into Hamilton's canonical form. The nature of the solutions depends on the eigen-structure of the system matrix: the null eigenvalues give rise to the central, or Saint-Venant's solutions and the non-vanishing eigenvalues lead to extremity solutions, which decay exponentially away from the beam's ends.

For thin-walled beam problems, both central and extremity solutions are necessary to obtain accurate predictions. Correct boundary conditions based on the weak form formulation are derived. The contribution of each extremity mode is evaluated from the boundary conditions directly. When the dominant modes are used, two-dimensional plate or shell solutions are recovered.

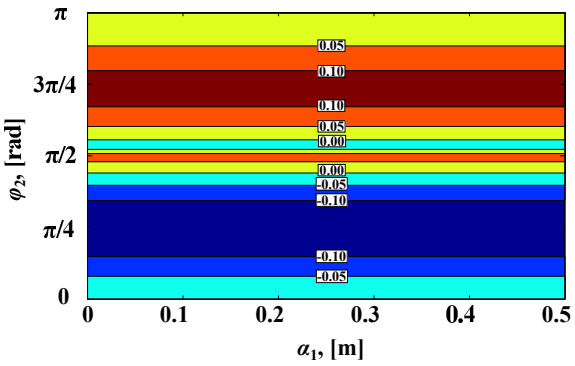

Figure 23: Resultant shear force component, N_{12}^+ ($\mathrm{N{\cdot}m^{-1}}$), present solution, $n_e = 0$.

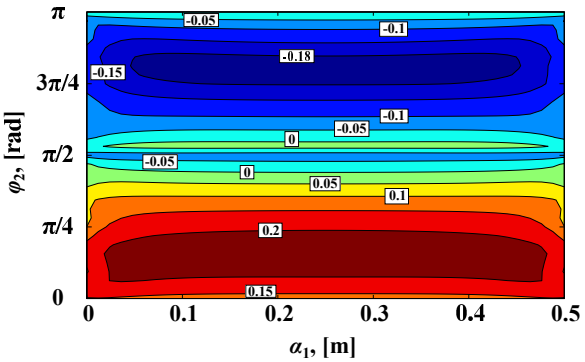

Figure 24: Resultant shear force component, N_{12}^{+} (N·m^{-1}), present solution, $n_e = 2$.

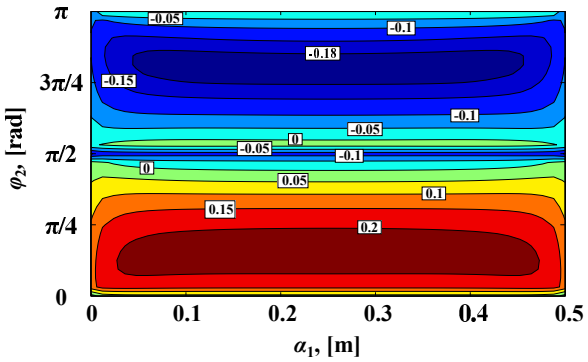

Figure 25: Resultant shear force component, N_{12}^{+} (N·m^{-1}), ABAQUS.

Numerical examples have been presented to demonstrate the capabilities of the proposed approach. Its accuracy was assessed by comparing its predictions against those of a two-dimensional plate and shell FEM analysis and other beam theories. As illustrated by the I-beam problem, Vlasov's theory includes the extremity solution associated with the lowest eigenvalue only. However, the present approach shows that the lowest three modes contribute to the beam's response significantly. For the hollow flange beam, the present predictions agrees with those obtained from the generalized beam theory. Curved thin-walled sections made of composite materials has been investigated in the third example.

The proposed approach involves two steps: *(1)* the sectional analysis and *(2)* the one-dimensional beam analysis. The sectional analysis provides the 6×6 sectional stiffness matrix and a set of symplectically orthogonal decaying modes. For beams subjected to load or constraints at end sections only, closed form one-dimensional beam solutions are obtained. Of course, the proposed approach can applied to beams with any loading conditions if finite element discretization is used along the beam's axis.

The proposed approach could be generalized to naturally curved and twisted thin-walled beams; buckling and post-buckling problems could be investigated as well.

A Matrices $\underline{\underline{A}}_1$, $\underline{\underline{A}}_2$ and $\underline{\underline{B}}$

Matrices $\underline{\underline{A}}_1$ and $\underline{\underline{A}}_2$, both of size 9×6, are defined as follows

$$\underline{\underline{A}}_1 = \begin{bmatrix} 1 & 0 & 0 & 0 & 0 & 0 \\ 0 & 0 & 0 & 0 & 0 & 0 \\ 0 & 1 & 0 & 0 & 0 & 0 \\ 0 & 0 & 1 & 0 & 0 & 0 \\ 0 & 0 & 0 & 0 & 0 & 0 \\ 0 & 0 & 0 & 0 & 1 & 0 \\ 0 & 0 & 0 & 0 & 0 & 0 \\ 0 & 0 & 0 & -1 & 0 & 0 \\ 0 & 0 & 0 & 0 & 0 & 0 \end{bmatrix}, \quad \underline{\underline{A}}_2 = \begin{bmatrix} 0 & 0 & 0 & 0 & 0 & 0 \\ 0 & 1 & 0 & 0 & 0 & 0 \\ 1 & 0 & 0 & 0 & 0 & 0 \\ 0 & 0 & 0 & 0 & 0 & 0 \\ 0 & 0 & 1 & 0 & 0 & 0 \\ 0 & 0 & 0 & 0 & 0 & 0 \\ 0 & 0 & 0 & -1 & 0 & 0 \\ 0 & 0 & 0 & 0 & 1 & 0 \\ 0 & 0 & 0 & 0 & 0 & 0 \end{bmatrix}. \tag{19}$$

Matrix $\underline{\underline{B}}$, also of size 9×6, features a single non-vanishing entry, $1/\rho$, in location $(2, 3)$.

B Hamiltonian matrices

Matrix $\underline{\underline{\mathcal{H}}}$, of size $2n \times 2n$, is said to be Hamiltonian if it satisfies the following property

$$(\underline{\underline{\mathcal{J}}}\,\underline{\underline{\mathcal{H}}})^T = \underline{\underline{\mathcal{J}}}\,\underline{\underline{\mathcal{H}}}, \tag{20}$$

where skew-symmetric matrix $\underline{\underline{\mathcal{J}}}$ is defined as

$$\underline{\underline{\mathcal{J}}} = \begin{bmatrix} \underline{\underline{0}}_{n\times n} & \underline{\underline{I}}_{n\times n} \\ -\underline{\underline{I}}_{n\times n} & \underline{\underline{0}}_{n\times n} \end{bmatrix}. \tag{21}$$

Note the following properties of matrix $\underline{\underline{\mathcal{J}}}$: $\underline{\underline{\mathcal{J}}}^T = -\underline{\underline{\mathcal{J}}}$, $\underline{\underline{\mathcal{J}}}\,\underline{\underline{\mathcal{J}}}^T = \underline{\underline{\mathcal{I}}}$.

Property (20) implies that the most general form of a Hamiltonian matrix is

$$\underline{\underline{\mathcal{H}}} = \begin{bmatrix} \underline{\underline{A}} & \underline{\underline{B}} \\ \underline{\underline{C}} & -\underline{\underline{A}}^T \end{bmatrix}, \tag{22}$$

where matrices $\underline{\underline{A}}$, $\underline{\underline{B}}$, and $\underline{\underline{C}}$ are of size $n \times n$ and matrices $\underline{\underline{B}}$ and $\underline{\underline{C}}$ are symmetric.

C Matrix function $\underline{\underline{\mathcal{G}}}_c$

Matrix function $\underline{\underline{\mathcal{G}}}_c(\alpha_1)$, of size 12×12 is defined as

$$\underline{\underline{\mathcal{G}}}_c(\alpha_1) = \begin{bmatrix} \underline{\underline{\mathcal{C}}}^{-1}(\alpha_1) & \underline{\underline{\mathcal{O}}}(\alpha_1) \\ \underline{\underline{0}} & \underline{\underline{\mathcal{C}}}^T(\alpha_1) \end{bmatrix}, \tag{23}$$

where sub-matrices $\underline{\underline{\mathcal{C}}}$ and $\underline{\underline{\mathcal{O}}}$, both of size 6×6, have the following form

$$\underline{\underline{\mathcal{C}}}(\alpha_1) = \underline{\underline{I}} + \alpha_1 \tilde{\mathcal{K}}^*, \tag{24a}$$

$$\underline{\underline{\mathcal{O}}}(\alpha_1) = \underline{\underline{S}}^*\alpha_1 + \frac{1}{2}\left(-\tilde{\mathcal{K}}^*\underline{\underline{S}}^* + \underline{\underline{S}}^*\tilde{\mathcal{K}}^{*T}\right)\alpha_1^2 - \frac{1}{6}\tilde{\mathcal{K}}^*\underline{\underline{S}}^*\tilde{\mathcal{K}}^{*T}\alpha_1^3. \tag{24b}$$

References

[1] V.Z. Vlasov. *Thin-walled Elastic Beams*. Office of Technical Services, US Department of Commerce, Washington, D.C., 1961.

[2] S.U. Benscoter. A theory of torsion bending for multicell beams. *Journal of Applied Mechanics*, 21:25–34, 1954.

[3] A. Gjelsvik. *The Theory of Thin Walled Bars*. Wiley, New York, 1981.

[4] H. Shakourzadeh, Y.Q. Guo, and J.-L. Batoz. A torsion bending element for thin-walled beams with open and closed cross sections. *Computers & Structures*, 55(6):1045–1054, 1995.

[5] N.R. Bauld and L.S. Tzeng. A Vlasov theory for fiber-reinforced beams with thin-walled open cross-sections. *International Journal of Solids and Structures*, 20(3):277–297, 1984.

[6] R. Chandra and I. Chopra. Experimental and theoretical analysis of composite I-beams with elastic couplings. *AIAA Journal*, 29(12):2197–2206, 1991.

[7] X.X. Wu and C.T. Sun. Simplified theory for composite thin-walled beams. *AIAA Journal*, 30(12):2945–2951, 1992.

[8] E. Carrera and G. Giunta. Refined beam theories based on a unified formulation. *International Journal of Applied Mechanics*, 02(1):117–143, 2010.

[9] V.L. Berdichevsky. On the energy of an elastic rod. *Prikladnaya Matematika y Mekanika*, 45(4):518–529, 1982.

[10] V.V. Volovoi and D.H. Hodges. Single- and multi-celled composite thin-walled beams. *AIAA Journal*, 40:960–965, 2003.

[11] W.B. Yu, D.H. Hodges, V.V. Volovoi, and E.D. Fuchs. A generalized Vlasov theory for composite beams. *Thin-Walled Structures*, 43(9):1493–1511, 2005.

[12] R. Schardt. *Verallgemeinerte Technische Biegetheorie*. Springer-Verlag, Berlin, 1989.

[13] J.M. Davies and P. Leach. First-order generalised beam theory. *Journal of Constructional Steel Research*, 31(2–3):187–220, 1994.

[14] P. Leach and J.M. Davies. An experimental verification of the generalized beam theory applied to interactive buckling problems. *Thin-Walled Structures*, 25(1):61–79, 1996.

[15] N. Silvestre and D. Camotim. First-order generalised beam theory for arbitrary orthotropic materials. *Thin-Walled Structures*, 40(9):755–789, 2002.

[16] P. Simão and L. Simões da Silva. A unified energy formulation for the stability analysis of open and closed thin-walled members in the framework of the generalized beam theory. *Thin-Walled Structures*, 42(10):1495–1517, 2004.

[17] D. Camotim, C. Basaglia, and N. Silvestre. GBT buckling analysis of thin-walled steel frames: A state-of-the-art report. *Thin-Walled Structures*, 48(10–11):726–743, 2010.

[18] R. Gonçalves, M. Ritto-Corrêa, and D. Camotim. A new approach to the calculation of cross-section deformation modes in the framework of generalized beam theory. *Computational Mechanics*, 46(5):759–781, 2010.

[19] V. Giavotto, M. Borri, P. Mantegazza, G. Ghiringhelli, V. Carmaschi, G.C. Maffioli, and F. Mussi. Anisotropic beam theory and applications. *Computers & Structures*, 16(1-4):403–413, 1983.

[20] A. Mielke. Saint-Venant's problem and semi-inverse solutions in nonlinear elasticity. *Archive of Rational Mechanics and Analysis*, 102:205–229, 1988.

[21] A. Mielke. Normal hyperbolicity of center manifolds and Saint-Venant's principle. *Archive of Rational Mechanics and Analysis*, 110:353–372, December 1990.

[22] W.X. Zhong. Plane elasticity problem in strip domain and Hamiltonian system. *Journal of Dalian University of Technology*, 4:373–384, 1991.

[23] O.A. Bauchau and S.L. Han. Three-dimensional beam theory for flexible multibody dynamics. *Journal of Computational and Nonlinear Dynamics*, 9(4):041011 (12 pages), 2014.

[24] S.L. Han and O.A. Bauchau. Nonlinear three-dimensional beam theory for flexible multibody dynamics. *Multibody System Dynamics*, 34(3):211–242, July 2015.

[25] S.L. Han and O.A. Bauchau. On the solution of Almansi-Michell's problem. *International Journal of Computers and Structures*, 2015. To appear.

[26] J.N. Reddy. *Mechanics of Laminated Composite Plates and Shells: Theory and Analysis*. CRC Press, Boca Raton, 2004.

[27] C. Lanczos. *The Variational Principles of Mechanics*. Dover Publications, Inc., New York, 1970.

[28] S.L. Han and O.A. Bauchau. On the Saint-Venant's problem for helicoidal beams. *Journal of Applied Mechanics*, 83(2):021009 (14 pages), 2016.

[29] S.L. Han and O.A. Bauchau. A novel, single-layer model for composite plates using local-global approach. *European Journal of Mechanics - A/Solids*, 2016. To appear.

[30] B. Fraeijs de Veubeke. *A Course in Elasticity*, volume 29. Springer-Verlag, New York, 1979.

[31] W.A Yao and Y.F. Sui. Symplectic solution system for Reissner plate bending. *Applied Mathematics and Mechanics*, 25(2):178–185, 2004.

[32] R.F. Vieira, F.B.E. Virtuoso, and E.B.R. Pereira. A higher order model for thin-walled structures with deformable cross-sections. *International Journal of Solids and Structures*, 51(3-4):575–598, 2014.

[33] K.J. Bathe. *Finite Element Procedures*. Prentice Hall, Inc., Englewood Cliffs, New Jersey, 1996.